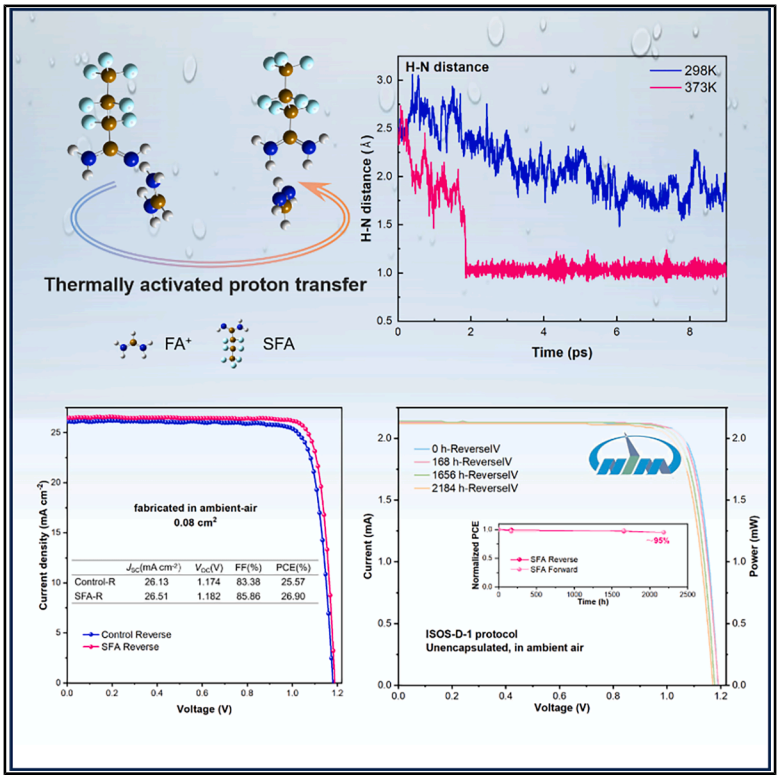
Joule

Article

Thermally activated proton transfer enables air-processed perovskite solar cells approaching 27%

Graphical abstract



Highlights

- A thermally activated proton-transfer strategy regulates perovskite crystallization
- Air-processed PSCs reach a PCE of 26.90%
- Unencapsulated PSCs achieve certified ambient-air storage stability

Authors

Yingying Yang, Zhineng Lan, Hao Huang, ..., Zhenhuang Su, Yingfeng Li, Meicheng Li

Correspondence

hhuang@ncepu.edu.cn (H.H.), suzh@sari.ac.cn (Z.S.), mcli@ncepu.edu.cn (M.L.)

In brief

Making high-performance perovskite solar cells in ordinary air is difficult because moisture and heat disrupt film formation. Here, a small molecular additive guides crystal growth at the start and then stabilizes the material during annealing, enabling highly efficient devices made outside a glovebox. The work shows that additive design can control both processing and stability at once, offering a practical path toward lower-cost, scalable perovskite solar manufacturing.

Yang et al., 2026, Joule *10*, 102579
July 15, 2026 © 2026 Elsevier Inc. All rights are reserved, including those for text and data mining, AI training, and similar technologies.
https://doi.org/10.1016/j.joule.2026.102579

CellPress

Please cite this article in press as: Yang et al., Thermally activated proton transfer enables air-processed perovskite solar cells approaching 27%, Joule (2026), https://doi.org/10.1016/j.joule.2026.102579

Joule

CellPress

Article

Thermally activated proton transfer enables air-processed perovskite solar cells approaching 27%

Yingying Yang,[1] Zhineng Lan,[1] Hao Huang,[1,*] Yan Chen,[2] Peng Cui,[1] Chuanmin Yao,[1] Luyao Yan,[1] Min Wang,[1] Changxu Sun,[1] Wenyuan Xiao,[1] Qiang Zhang,[1] Pengkun Zhu,[1] Shuxian Du,[1] Shujie Qu,[1] Zhenhuang Su,[3,*] Yingfeng Li,[1] and Meicheng Li[1,4,*]

[1]State Key Laboratory of Alternate Electrical Power System with Renewable Energy Sources, School of New Energy, North China Electric Power University, Beijing 102206, China

[2]Institute of Clusters and Low Dimensional Nanomaterials, School of Mathematics and Physics, North China Electric Power University, Beijing 102206, China

[3]Shanghai Synchrotron Radiation Facility, Shanghai Advanced Research Institute, Chinese Academy of Sciences, Shanghai 201204, China

[4]Lead contact

*Correspondence: hhuang@ncepu.edu.cn (H.H.), suzh@sari.ac.cn (Z.S.), mcli@ncepu.edu.cn (M.L.)

https://doi.org/10.1016/j.joule.2026.102579

CONTEXT & SCALE Transitioning perovskite solar cell (PSC) manufacturing from inert-gas gloveboxes to ambient air is a prerequisite for low-cost, high-throughput industrialization. However, a persistent "performance gap" remains between air-processed and glovebox-processed devices, primarily due to the synergistic degradation caused by atmospheric moisture and annealing heat. This work identifies that moisture-induced deprotonation of formamidinium (FA^+) is significantly accelerated by thermal stress. To address this, we introduce a thermally activated proton transfer strategy using a hydrophobic dipolar molecule, heptafluorobutyramidine (SFA). Unlike passive additives, SFA acts as a dynamic modulator: it shields moisture during deposition and actively stabilizes the lattice during annealing. This approach yields a certified efficiency of 26.74% and demonstrates high performance in large-area modules, providing a scientifically rigorous pathway for scalable, climate-resilient photovoltaic manufacturing.

SUMMARY

Ambient-air fabrication of perovskite solar cells (PSCs) is cost-effective, yet crystallization regulation under moisture invasion represents an urgent challenge. Here, we report a thermally activated proton-transfer strategy through hydrophobic dipolar heptafluorobutyramidine (SFA) to stage-specifically regulate perovskite crystallization. SFA first induces a porous PbI_2 scaffold that accelerates organic-salt infiltration and phase formation. Upon annealing, SFA undergoes a heat-triggered proton transfer with formamidinium (FA^+). In this process, SFA acts as a proton custodian to prevent volatile deprotonation, while the resulting protonated SFA^+ then helps stabilize FA-deficient local regions and passivate vacancy-related defects, thereby suppressing surface-associated decomposition and metallic Pb^0 formation. Consequently, we achieved a power conversion efficiency (PCE) of 26.90% (certified 26.74%) for air-processed PSCs. The unencapsulated device maintained >95% of initial efficiency after 2,000 h of storage in ambient air and 91% after 1,100 h of operation under 1-sun illumination in N_2 atmosphere.

INTRODUCTION

Metal halide perovskite solar cells (PSCs) have attracted significant attention as a promising photovoltaic technology with tremendous advances in power conversion efficiency (PCE), owing to the absorber's advantages of high carrier mobility, long carrier diffusion length, adjustable band gap, and so on.[1–3] The α-phase formamidinium lead iodide (α-$FAPbI_3$) exhibits an impressive band gap, becoming the priority as the photoactive material for fabricating high-efficiency PSCs.[4–7] However, α-$FAPbI_3$ is not thermodynamically stable at room temperature (RT) and readily transforms into a non-perovskite phase.[8] Besides, polytype intermediate non-photoactive phases can readily occur during the crystallization process, undermining its photovoltaic performance.[9] The vast majority of record-breaking PCEs have been achieved using devices fabricated in

All rights are reserved, including those for text and data mining, AI training, and similar technologies.

Please cite this article in press as: Yang et al., Thermally activated proton transfer enables air-processed perovskite solar cells approaching 27%, Joule (2026), https://doi.org/10.1016/j.joule.2026.102579

inert-gas gloveboxes that strictly exclude atmospheric moisture.[10–12] Transitioning from controlled environments to ambient-air manufacturing is therefore an indispensable prerequisite for realizing the commercial potential of PSC technology.[13–15]

The moisture in ambient air can induce disruptive phase transitions, destruction of the crystal framework, and escape of the organic component.[16,17] This serious impact can occur throughout the entire crystallization process, including nucleation during the coating process and crystal growth during the annealing process under high temperature.[8,18] It has been shown that the moisture induces the formation of the non-perovskite phase of δ-$FAPbI_3$ through impacting the DMSO-based complex, which hinders the formation of α-$FAPbI_3$.[13,19] To remove or reduce the solvent-induced moisture absorption, Hui et al. utilized an ionic liquid to form a vertically aligned lead iodide thin film with numerous nanometer-scale ion channels that can facilitate the permeation of formamidinium iodide (FAI) into the lead iodide thin films for fast and robust transformation to α-$FAPbI_3$.[20] Beyond the solvent-related detrimental issues, the defects, especially the vacancy defects at the surface and grain boundary, can promote the absorption of water molecules and trigger the hydration of the perovskite, eventually leading to the degradation of the material.[21] Additives such as guanabenz acetate salt have been proposed to passivate both the cation and anion vacancies, thus blocking the perovskite hydration and allowing the crystallization of a high-quality perovskite film in ambient air.[8]

However, this understanding and modulation mainly focus on the single stage of crystallization, such as the $FAPbI_3$ formation reaction, nucleation, or the first stage of crystal growth, which shows a limited effect on the continuous perovskite crystallization.[22–24] Moreover, these approaches often concentrate on "moisture exclusion" via hydrophobic additives or solvent engineering, overlooking a critical failure mechanism: the synergistic destruction triggered by the coupling of residual moisture and annealing heat. While moisture ingress at RT is detrimental, the high temperatures required for crystallization kinetically accelerate the deprotonation of formamidinium (FA^+) ions by water molecules. This process leads to the volatile escape of ammonia and the irreversible collapse of the perovskite lattice into the non-photoactive δ-phase.[25,26] Consequently, stabilizing the FA^+ sublattice against this "thermal-moisture" stress represents the central bottleneck in obtaining high-quality air-processed perovskite films.

In this work, we propose a thermally activated proton-transfer strategy by employing heptafluorobutyramidine (SFA) to stage-specifically modulate perovskite crystallization. During the initial film deposition, its fluorinated tail creates a hydrophobic barrier and induces a porous PbI_2 scaffold, promoting rapid organic-salt permeation. Subsequently, as the temperature increases, SFA undergoes a heat-triggered proton transfer with FA^+. In this active state, SFA acts as a "proton custodian," effectively outcompeting water molecules for protons to prevent volatile FA loss. The resulting protonated SFA^+ then helps stabilize FA-deficient local regions and passivate vacancy-related defects, thereby suppressing surface-associated decomposition and metallic Pb^0 formation. Benefiting from the perovskite film's excellent optoelectronic properties, the devices demonstrate robust performance. PSCs fabricated within a relative humidity (RH) range of 20%–55% (aperture area: 0.08 cm^2) all achieve PCEs exceeding 26%, with a champion value of 26.90% (certified 26.74%). Encouragingly, devices with aperture areas of 1 and 8.2 cm^2 achieve PCEs of 25.35% and 21.03%, respectively. Furthermore, unencapsulated devices exhibit exceptional durability, retaining >95% of their initial PCE after 2,000 h of storage in ambient air and maintaining 91% of their initial efficiency after 1,100 h of continuous operation under illumination (≈50°C) in a N_2 atmosphere.

RESULTS

Thermally activated proton transfer

The perovskite film was deposited via a two-step spin-coating method in ambient air, with its formation typically involving sequential processes: reaction, nucleation, crystallization, and secondary crystallization.[27] The crystallization is normally activated by high temperature. Given that ambient moisture inevitably interferes perovskite crystallization in its detailed processes, especially coupling with the function of high temperature (Figures S1 and S2),[28,29] we designed a thermally activated proton-transfer strategy through a hydrophobic SFA to conduct stage-specific regulation of perovskite crystallization. Figures S3 and S4 present the molecular structure of SFA and its surface electrostatic potential diagram. The SFA molecule has a straight carbon skeleton composed of 4 carbon atoms as its core and can be divided into two segments based on the position of functional groups. One segment is the heptafluorobutyl end with fluorine atoms substituted with extremely strong hydrophobicity and electron-attracting properties, which can reduce the overall electron cloud density of the molecule.[30] The other end is the amidine. Because the lone pair electrons of the nitrogen atom in the amidine can participate in the formation of hydrogen bonds or proton transfer, the amidine will become an electron-deficient region and the reaction active site of the entire molecule.[31] The strongly hydrophobic heptafluorobutanyl end is expected to create a hydrophobic protective layer that blocks the erosion of perovskite by moisture in the air throughout the entire process from the PbI_2 stage to complete film formation (Figure S5). Besides, the obvious difference in electronegativity of heptafluorobutanyl and amidine can support the interaction between the amidine end of the SFA and FA^+ in the perovskite structure, such as hydrogen bonds and further proton transfer (Figure S6).[32] In order to gain a deeper understanding of the interaction between SFA and FA^+, we simulated thermodynamic processes including hydrogen bond formation and proton transfer. The binding energy of hydrogen bonds expressed by Gibbs free energy is −12.32 kilocalories per mole at RT (Figure 1A), indicating that the combination is thermodynamically stable. The calculation results also show that the process of proton transfer between SFA and FA^+ is an endothermic process, which can be activated by high temperature for annealing in the perovskite film preparation. To theoretically probe the proton-transfer reaction between FA^+ and SFA during the annealing crystallization process, we conducted a calculation of *ab initio* molecular dynamics (AIMD) to track the proton-transfer

Please cite this article in press as: Yang et al., Thermally activated proton transfer enables air-processed perovskite solar cells approaching 27%, Joule (2026), https://doi.org/10.1016/j.joule.2026.102579

CellPress

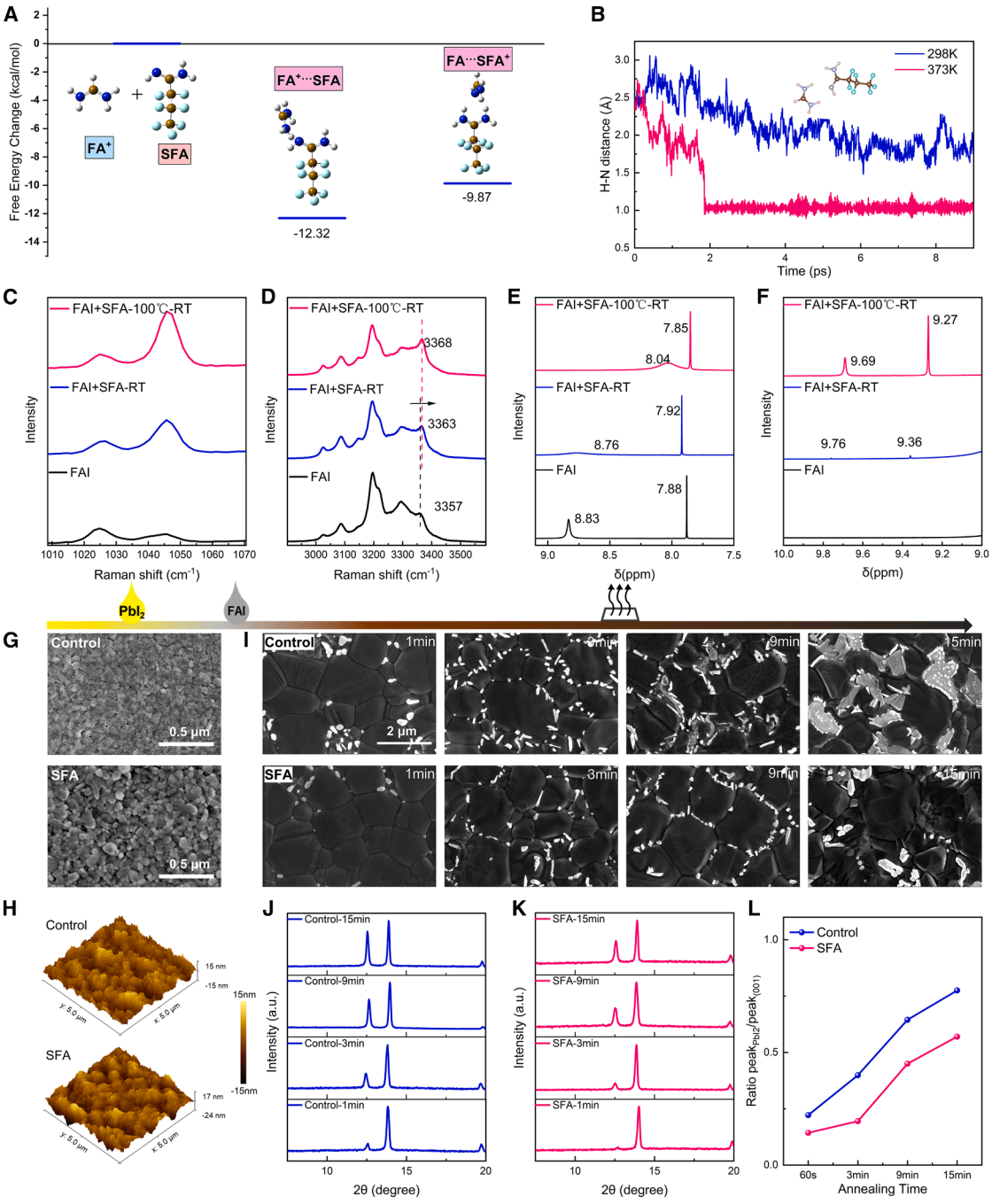


Figure 1. Thermally activated proton-transfer mechanism

(A) Calculated Gibbs free energies for the proton-transfer process between FA^+ and SFA.

(B) Time evolution of H–N intermolecular distance from molecular dynamics simulations. The H is from the $–NH_2$ group of FA^+, and the N is from the –NH group of SFA.

(C and D) Raman spectra, showing the vibrational peaks of different samples in characteristic wavenumber regions, respectively. The "FAI + SFA-RT" sample was the mixture of FAI and SFA. The "FAI + SFA-100°C-RT" sample was first heated at 100°C for 5 min and then cooled to RT and then measured.

(E and F) Liquid-state NMR spectra, presenting the chemical shift information of ^1H in different samples. All samples were prepared following a procedure identical to that of (C) and (D), with the exception that they were dissolved in DMSO-d_6.

(G) Top-view SEM images of PbI_2 films without and with SFA.

(H) 3D AFM images of PbI_2 films without and with SFA.

(I) Top-view SEM images of perovskite films without and with SFA under different annealing times.

(J and K) XRD patterns of perovskite films without and with SFA under different annealing times.

(L) Peak intensity ratio of PbI_2/(001) of perovskite films without and with SFA under different annealing times.

Please cite this article in press as: Yang et al., Thermally activated proton transfer enables air-processed perovskite solar cells approaching 27%, Joule (2026), https://doi.org/10.1016/j.joule.2026.102579

process at different temperatures. Figure 1B shows that a proton is hard to transfer from the $-NH_2$ of FA^+ to the –NH of SFA at 298 K; however, this proton transfer can be achieved within an extremely short period of 2 ps at 373 K and subsequently maintain a stable binding state. This indicates that the high-temperature conditions during annealing are favorable for proton transfer. The protonated SFA^+ after proton transfer can be thermodynamically stabilized at FA-vacancy-containing local sites (Figure S7), suggesting a favorable local defect-passivation effect. The passivated local vacancy environment can further hinder the formation of neighboring I^- vacancies (Figure S8).

To further explore the proton transfer between FA^+ and SFA, we used Raman spectroscopy tests on the powders of FAI, the mixture of FA^+ and SFA at RT, and the mixture after heating and subsequent cooling (Figures 1C and 1D). Firstly, we found that compared with the FAI sample, after mixing FAI and SFA, the intensities of the C–N backbone vibration peak at 1,045 cm^{-1} wavenumbers are enhanced, while the intensity of the N–H stretching vibration peak dominated by the peak at 3,197 cm^{-1} wavenumbers decreased significantly, and the peak at the 3,357 cm^{-1} wavenumbers position is enhanced and shifts toward higher wavenumbers (3,363 cm^{-1} wavenumbers). This indicates the interaction of hydrogen bonds between the $-NH_2$ of FA^+ and the –NH of SFA, which breaks the symmetrical and stable state of FA^+, increasing the polarizability of the C–N bond and the N–H bond during the vibration process and leading to an increase in the tensile vibration frequency of N–H. After further heating and cooling, the peak intensity at 1,045 cm^{-1} further increased, while the peak at 3,197 cm^{-1} further decreased, and the peak at 3,363 cm^{-1} further shifted to 3,368 cm^{-1} with increased intensity. These changes should be related to the formation of a new hydrogen-bonding configuration after heating, consistent with a proton-transfer-induced reorganization of the local N–H bonding environment.[33,34]

In addition to using Raman spectroscopy to track the reorganization of local vibrations and bonding environments, we also conducted liquid ^1H nuclear magnetic resonance (NMR) spectroscopy to characterize the FA^+, the mixture of FA^+ and SFA, in order to reflect the redistribution of proton chemical environments (Figures 1E and 1F). Initially, the spectrum of pure FAI at RT displays two characteristic peaks at 8.83 and 7.88 ppm, which are attributed to the $-NH_2$ protons of FA^+. When FAI and SFA are mixed at RT, one of the signal peaks shifts from 8.83 to 8.76 ppm, and the signal peak broadens, and the corresponding intensity decreases. Meanwhile, the other signal peak shifts from 7.88 to 7.92 ppm. The deformation and shift of this peak provide evidence for the formation of a hydrogen-bonded complex between the $-NH_2$ group of FA^+ and the –NH group of SFA.[35] In addition, the appearance of weak new peaks at positions 9.36 and 9.76 ppm might be caused by weak proton transfer at RT. When the mixture was heated and then cooled, the weak new peaks shifted from 9.36 and 9.76 ppm to 9.27 and 9.69 ppm, with a significant increase in intensity, while the peaks at 8.76 and 7.92 ppm moved toward a higher field. These changes indicate that heating causes a redistribution of proton environments. Together with the Raman results, this supports the evolution from RT hydrogen bonding to a stronger proton-transfer-related state after heating (Note S1).

To further investigate this process in a more solid-state environment closer to perovskite, we conducted ^1H solid-state NMR tests on $FAPbI_3$, $FAPbI_3$ + SFA-RT, and $FAPbI_3$ + SFA-100°C-RT. The spectrum of pure $FAPbI_3$ could be fitted into two broad peak components, with the centers located at 7.97 and 7.08 ppm, respectively. The RT mixed samples showed peaks redistributed into two components at 7.51 and 6.84 ppm, moving overall to a higher field, but no obvious new low-field features were observed, which may indicate the local perturbations mediated by hydrogen bonds. By contrast, the mixture samples after thermal treatment showed an additional low-field component at 8.55 ppm, accompanied by two components at 7.61 and 6.85 ppm, suggesting that after thermal treatment, a new, more deshielded proton environment was formed. This solid-state evolution trend is qualitatively consistent with the results of liquid-state ^1H NMR and jointly supports a hydrogen bond-mediated, thermally activated proton transfer-related process (Figure S9).

After understanding the thermally activated proton-transfer process between FA^+ and SFA, we further explored the influence of SFA on the perovskite crystallization. As shown in the scanning electron microscopy (SEM) image of Figure 1G, after the addition of SFA, the original dense and smooth PbI_2 film became rough and porous, which can also be validated by the 3D image characterized by atomic force microscopy (AFM) (Figure 1H). In the AFM image, the pores of PbI_2 film became wider and deeper, and the surface roughness also increased from 4.17 to 4.75 nm (Figure S10). This loose and porous structure will facilitate the permeation of FAI into the PbI_2 thin films for fast and robust transformation to α-$FAPbI_3$ in ambient condition.[36] From the SEM images of control perovskite films and SFA perovskite films obtained at different annealing times, it can be observed that at 1 min of annealing, both types of films exhibit dense grains. As the annealing time increases, we observe the increment of PbI_2 mainly located at the grain boundary, indicating the perovskite crystallization accompanied by the perovskite decomposition (Figure 1I). This perovskite decomposition mainly results from the escape of cations under the combined function of moisture and high temperature in the ambient air environment.[29,37] Compared with the control perovskite film, the SFA-film shows a significant reduction in the residual amount of PbI_2 at different stages of the annealing process, indicating that the decomposition of perovskite was effectively hindered. This is related to the hydrophobic effect of SFA and the proton transfer, which inhibits the reaction between FA^+ and moisture in the air, thereby reducing the escape of FA^+. The result of X-ray diffraction (XRD) in Figures 1J and 1K also synchronously shows the phenomenon of PbI_2 increase as the annealing time increases. To show in detail the inhibitory effect of SFA on the escape of FA^+, we extracted the peak ratio of PbI_2/perovskite (001) of both perovskite films with different annealing times. As shown in Figure 1L, although the peak ratio of PbI_2/perovskite (001) of both films shows an increasing tendency as the annealing time increases, the peak ratio of PbI_2/perovskite (001) of SFA-film is obviously gradually slower, and the ratio value is smaller than that of the control perovskite film under the same annealing time.

Stage-specific crystallization regulation mechanism

The *in situ* photoluminescence (PL) was further conducted to investigate the perovskite crystallization properties and analyze

Please cite this article in press as: Yang et al., Thermally activated proton transfer enables air-processed perovskite solar cells approaching 27%, Joule (2026), https://doi.org/10.1016/j.joule.2026.102579

the influence of SFA on them. The spin-coating process after dropping the ammonium solvent and the following annealing process have been monitored in real-time. As shown in Figures 2A–2C, during the spin-coating process, both films show similar changes, with the PL intensity increasing first, which may result from the $FAPbI_3$ nucleation, and then decreasing, which may result from the solvent phase transformation.[38] It is notable that the PL intensity climbing stage of PbI_2 with SFA occurs significantly earlier than that of the control PbI_2 film, and the high-level PL intensity of PbI_2 with SFA can also maintain a longer period. This rapid PL intensity climbing suggests the accelerated nucleation, which should be due to the promoted solid-liquid reaction between PbI_2 and organic ammonium salts.[39] This longer maintenance of high-level PL intensity may indicate the weakened interference from moisture by SFA. In addition, the *in situ* humidity-aging PL test results of the film that rapidly nucleates based on the anti-solvent effect can more clearly demonstrate the protective effect of SFA on the perovskite intermediate phase (Figures S11 and S12). The water contact angle measurements of the perovskite films further confirmed the enhanced moisture resistance conferred by the SFA modification (Figure S13).

We further monitored the *in situ* spectra of the films during the annealing process in ambient air. As shown in Figures 2D–2F, the crystallization process can roughly be divided into two stages.[40] The stage I corresponds to the reformation and the dissolution of perovskite nuclei, which can be demonstrated by the rapid increase and subsequent decrease in PL intensity. Stage II involves the crystallization and secondary crystallization, corresponding to the rapid recovery and continuous enhancement of PL intensity. Compared with control film, the SFA-film exhibits a more persistent and intense nucleation reformation process and enters the nucleation growth and crystallinity enhancement process earlier. The subsequent growth of crystal nuclei and the rate of crystallinity enhancement are also significantly faster than those of the control film, with a maintained higher intensity. This optimized crystallization kinetics is similarly reflected in the evolution of the crystal structure. *In situ* grazing-incidence wide-angle X-ray scattering (GIWAXS) analysis during annealing reveals that SFA modifies the transient phase-evolution pathway and accelerates the conversion toward the photoactive phase. Although a stronger δ-related transient signal is observed at the very early stage for the SFA-film, this behavior is consistent with a faster transient conversion process. Ultimately, the modified film undergoes a more complete phase transition and exhibits significantly fewer residual δ-phase impurities after annealing, further supporting the positive role of SFA in enhancing film quality (Figures 2G–2I and S14–S16; Note S2).

Based on the above analysis, we presented a schematic diagram of the mechanism by which SFA regulates the crystallization process of perovskite (Figure 2J). Firstly, introducing SFA makes PbI_2 film looser with more porous, which facilitates the permeation of FAI and promotes the initial conversion process under ambient conditions. As the annealing starts, corresponding to the nucleation and primary crystallization, SFA undergoes a heat-triggered proton transfer with FA^+. The formation of protonated SFA^+ and reshaped interaction between SFA and FA^+ can promote the conversion of δ-phase to the photoactive phase. As the annealing stage proceeds, corresponding to the crystal growth and secondary crystallization, the protonated SFA^+ can passivate vacancy-related defects and stabilize FA-deficient local regions, thereby hindering the perovskite decomposition that accompanies the annealing process. This crystallization regulatory mechanism that almost runs through the entire process has specific modes of action at different crystallization stages. These crystallization regulations and defect passivations synergistically contribute to achieving high-quality perovskite film (Figures S17–S19; Note S3).

High-performance air-processed PSCs

To study the influence of SFA on the perovskite films prepared in the ambient air, we conducted a systematic comparison of samples prepared under three distinct conditions: in a nitrogen glovebox (N_2-film), in ambient air (air-film), and in ambient air with the SFA additive (air + SFA-film). X-ray photoelectron spectroscopy (XPS) analysis revealed the chemical states of the components (Figure 3A). By integrating the characteristic peaks of Pb^0 and Pb^{2+} and calculating their relative ratio, the Pb^0/Pb ratio of N_2-film was determined to be 4.1%. This ratio increased to 7.7% in the air-film, indicating exacerbated perovskite decomposition and metallic lead formation during ambient air fabrication. Notably, the air + SFA-film exhibited a significantly lower Pb^0/Pb ratio of only 3.1%, comparable to the level observed in the N_2-film. We also analyzed the XPS atomic ratios of I/Pb and N/Pb and normalized them to the N_2-film (Figure 3B; Note S4). Relative to the N_2-film, the air-film shows reduced N/Pb and altered I/Pb, whereas the air + SFA-film exhibits recovery trends in both ratios. Taken together, the reduced Pb^0/Pb ratio and the recovery trends of the XPS-derived I/Pb and N/Pb ratios support that SFA alleviates air-induced compositional degradation during film formation. The energy-dispersive spectroscopy (EDS) measurement shows that the relevant elements are evenly distributed in each film, while the semi-quantitative EDS analysis on N/Pb gives a trend consistent with that of XPS (Figures S20–S23; Note S5).[11] Time-of-flight secondary ion mass spectrometry (ToF-SIMS) depth profiling shows that SFA is distributed throughout the perovskite film. At the interface, especially near the bottom perovskite/SnO_2 interface, there is a more pronounced enrichment (Figure S24). This distribution characteristic may result from the preparation path of introducing SFA into the PbI_2 precursor layer.

This improvement in intrinsic material quality directly manifests in the photoelectric properties of the films. PL mapping showed a significantly enhanced fluorescence intensity for the SFA-film (Figure 3C). Time-resolved PL (TRPL) measurements indicated an extension of the carrier lifetime from 0.65 to 0.95 μs (Figure 3D; Table S1).[41] The PL quantum yield (PLQY) increased from 2.578% to 4.682% (Figure 3E). Combined with the reduction in defect density determined by the space-charge-limited-current (SCLC) method from 2.43×10^{15} to 2.14×10^{15} cm^{-3} (Figure S25), these results collectively verify the synergistic effect of reduced defect state density and suppressed non-radiative recombination. The suppressed non-radiative recombination can also be validated by the results of dark current tests, electrochemical impedance spectroscopy, and

Please cite this article in press as: Yang et al., Thermally activated proton transfer enables air-processed perovskite solar cells approaching 27%, Joule (2026), https://doi.org/10.1016/j.joule.2026.102579

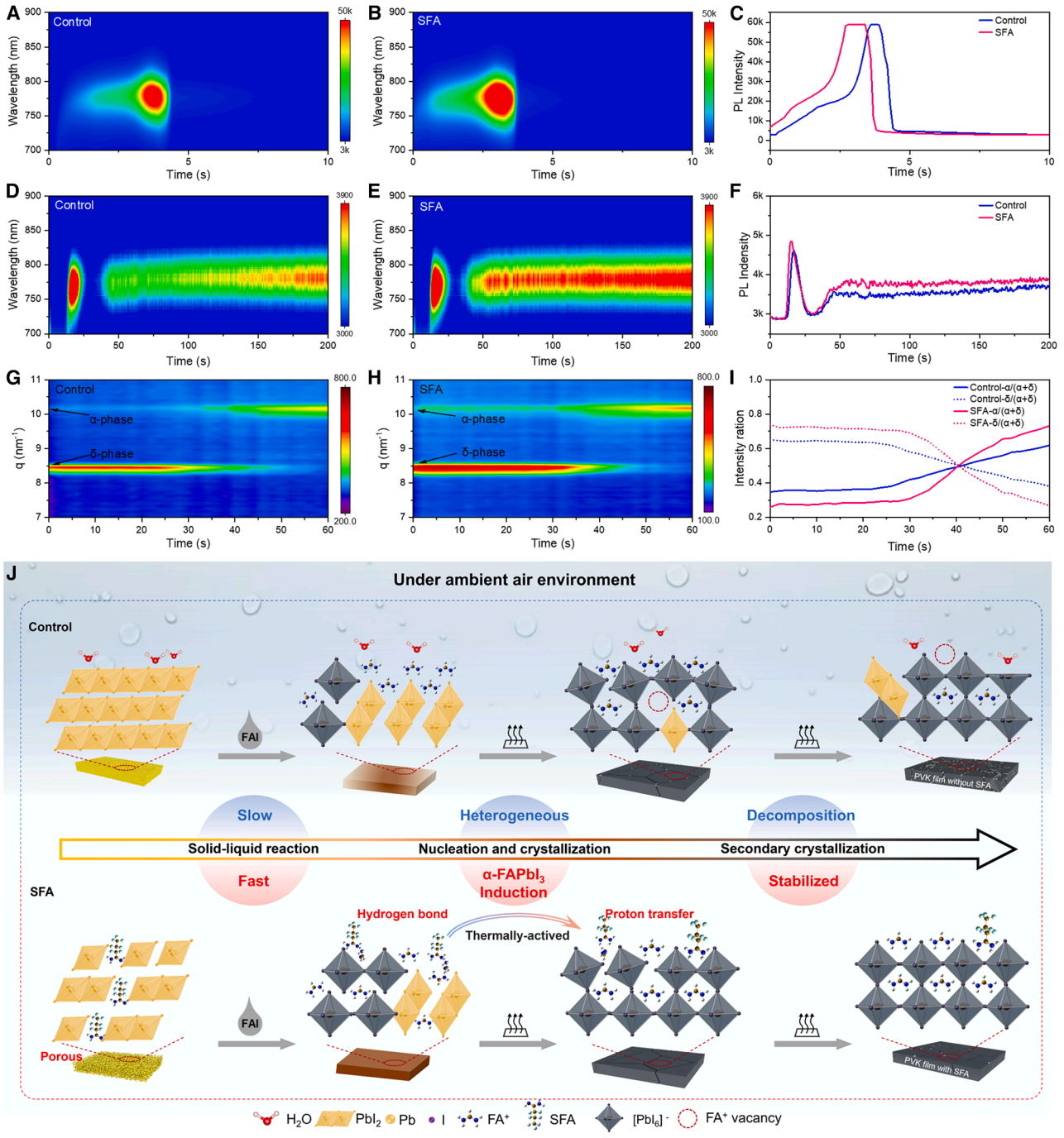


Figure 2. Multistage regulation of the perovskite crystallization process

(A–C) *In situ* PL spectra of perovskite films without and with SFA during the spin-coating process.

(D–F) *In situ* PL spectra of perovskite films without and with SFA during the annealing process.

(G and H) Time evolution of GIWAXS intensity along q_z direction for the perovskite films without and with SFA during the annealing process.

(I) Temporal evolution of the relative intensity ratio of the α-phase to the sum of (PbI_2 + δ-phase + α-phase).

(J) Schematic diagrams of the crystallization mechanism of perovskite films without SFA and with SFA in ambient air.

electroluminescence (Figures S26–S28; Table S2). We further characterize the voltage loss decomposition and quasi-fermi level splitting (QFLS) under variable light intensity to primarily evaluate the influence of SFA on PSCs physical properties. The results in Figures S29 and S30 showed that the incorporation of SFA induced a larger QFLS and reduced voltage loss. In detail,

Please cite this article in press as: Yang et al., Thermally activated proton transfer enables air-processed perovskite solar cells approaching 27%, Joule (2026), https://doi.org/10.1016/j.joule.2026.102579

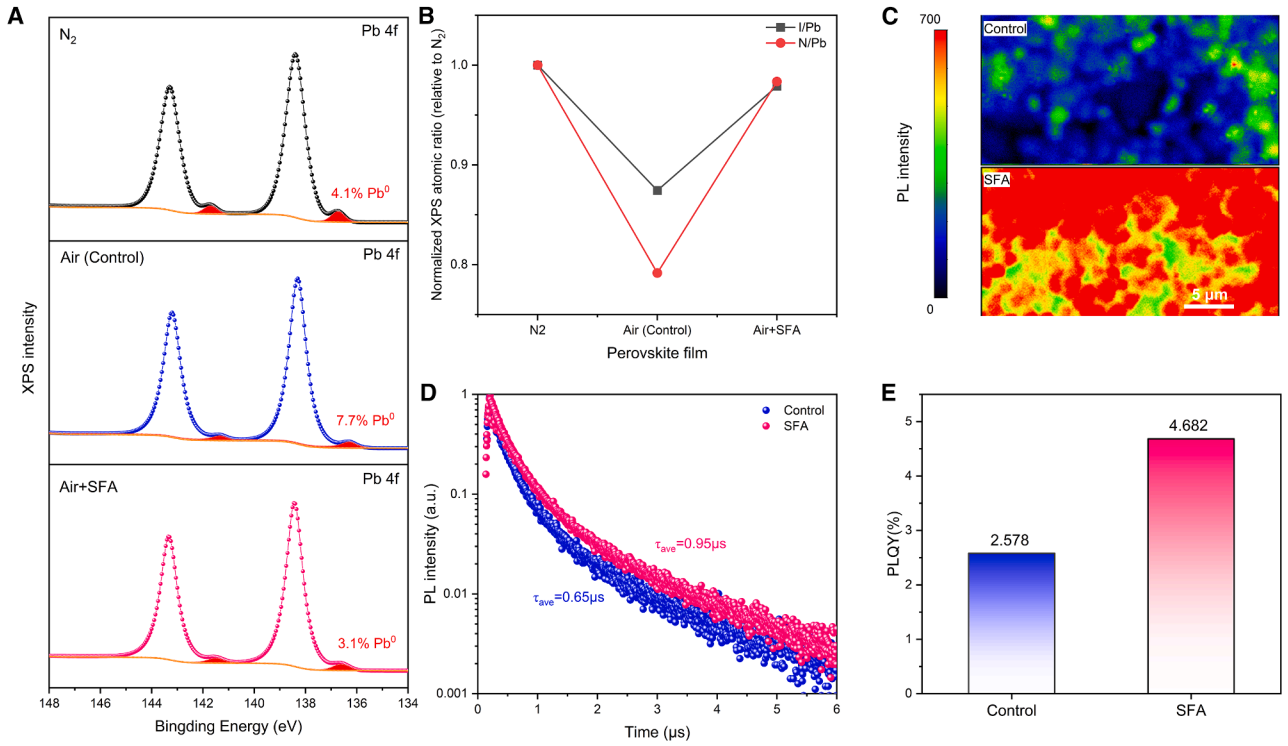


Figure 3. Improvement of the properties of perovskite films

(A) The XPS spectra of Pb 4f for the perovskite films prepared in N_2 (denoted as "N_2"), in ambient air (denoted as "air"), and in ambient air with SFA stabilizer (denoted as "air + SFA"). The orange curve denotes the baseline, and the red curve with color filling represents the ratio of the Pb^0 signal.

(B) The relative N/Pb and I/Pb atomic ratios normalized to the N_2 sample.

(C) PL mapping of perovskite films without SFA and with SFA.

(D) TRPL spectra of perovskite films without SFA and with SFA.

(E) PLQY of perovskite films without SFA and with SFA.

the $q\Delta V_3$, which represents non-radiative recombination loss, decreased from 94.59 to 79.15 mV.

Based on the high-quality perovskite film obtained by SFA, we fabricated planar PSCs structured as fluorine-doped tin oxide (FTO)/SnO_2/perovskite/2-fluorophenylethylammonium iodide (o-F-PEAI)/2,2′,7,7′-tetrakis[N,N-di(4-methoxyphenyl)amino]-9-9′-spirobifluorene [spiro]/Au in ambient air. By correlating the SFA-concentration-dependent structural evolution, morphological evolution, film optoelectronic properties, and photovoltaic performance, we determined a moderate amount of SFA that can reduce the residual PbI_2 in the perovskite films and improve the film optoelectronic quality (Figure S31). We then collected the photovoltaic parameters of 40 control PSCs and 40 SFA-PSCs, respectively. The SFA-PSCs achieve an impressive PCE of 26.90% with a small hysteresis, the corresponding short current density (J_{SC}) is 26.51 mA cm^{-2}, open circuit voltage (V_{OC}) is 1.182 V, and the fill factor (FF) is 85.86% (Figures 4A and S32; Table S3). The corresponding external quantum efficiency (EQE) spectrum is shown in Figure S33, yielding an integrated short circuit current density of 26.26 mA cm^{-2}, with a small difference from the value obtained from current-voltage (*J-V*) measurement. By contrast, the control PSCs only achieve a champion PCE of 25.57%, with a J_{SC} of 26.13 mA cm^{-2}, a V_{OC} of 1.174 V, and an FF of 83.38%. The FF improvement mainly results from the reduced non-radiative recombination loss (Figure S34). One of the best-performing SFA-PSCs was sent to an independent solar cell-accredited laboratory (National Institute of Metrology, China) for certification, achieving a PCE of 26.74% (Figure S35). In addition, the PCE of SFA-PSCs also exhibits a satisfactory reproducibility (Figure 4B), and the average PCE of SFA-PSCs was 26.16%, higher than that of control PSCs (24.59%). The corresponding V_{OC}, J_{SC}, and FF distributions are shown in Figure S36. A similar beneficial trend was also observed in one-step PSCs, where SFA-containing devices exhibited improved photovoltaic performance (Figure S37). Moreover, PSCs with an active area of 1 cm^2 were also prepared. The PCE for the best-performing SFA-PSC is 25.35%, superior to 24.61% for the control PSC (Figure 4C). We summarized the efficiency of efficient PSCs reported recently (Figures S38–S40; Tables S4–S6). We achieved a PCE of 26.90% for small-area devices and 25.35% for large-area devices, and both values are among the highest among the reported PSCs fabricated in ambient air. Upon further scaling up the device area, the SFA-mini module (8.2 cm^2) achieves a PCE of 21.03%, demonstrating the significant potential of our strategy on large-scale industrialization of PSCs (Figure S41; Note S6). Statistical distributions of the photovoltaic parameters for the 1.0 cm^2 PSCs and 8.2 cm^2 mini modules are provided in Figures S42

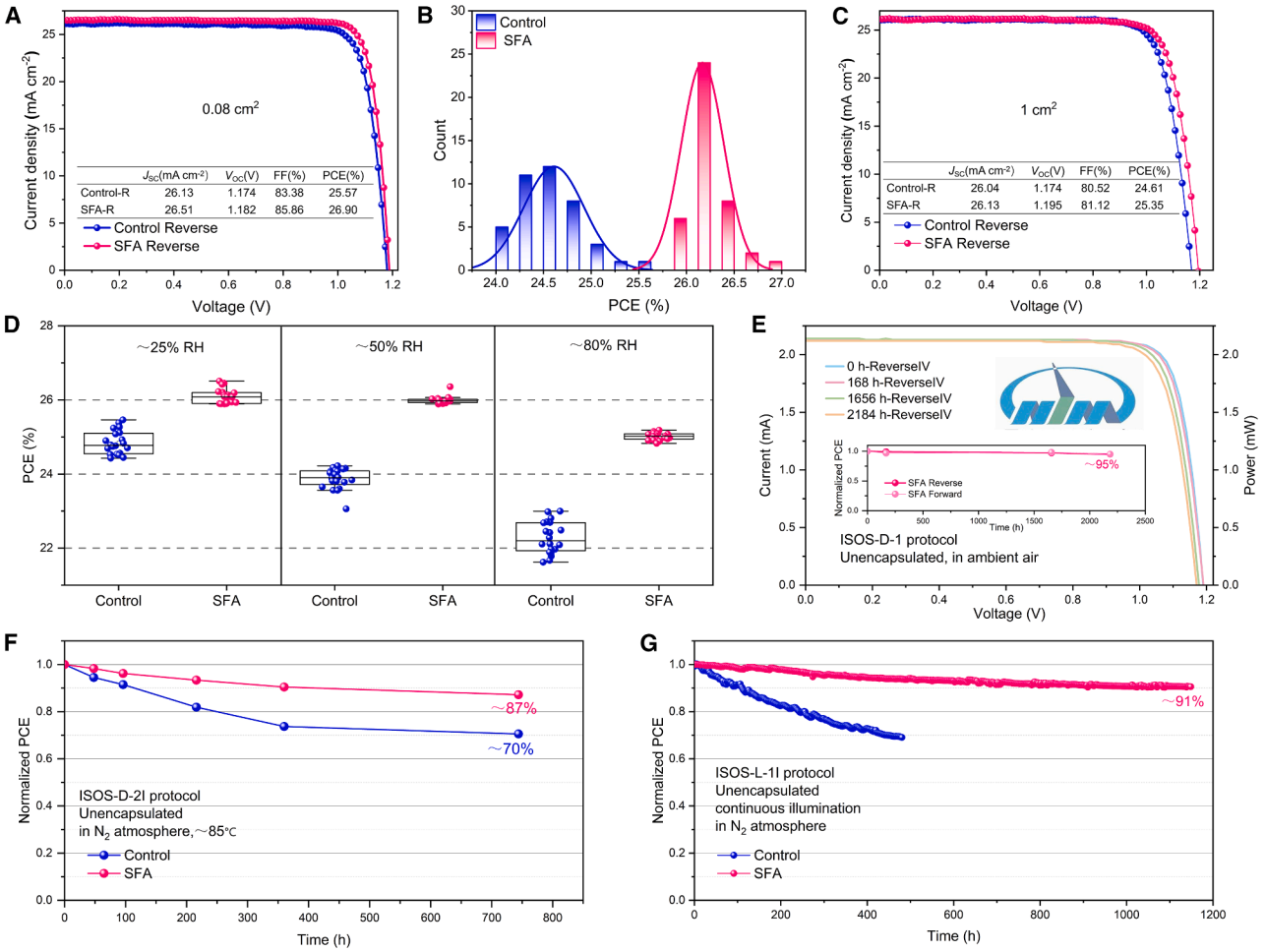


Figure 4. Photovoltaic performance of the PSCs fabricated in ambient air

(A) *J-V* curves of the champion control and SFA-PSCs with an aperture area of 0.08 cm^2.

(B) Distribution histograms of PCE value among 40 control and SFA-PSCs, respectively.

(C) *J-V* curves of the champion control and SFA-PSCs with an aperture area of 1 cm^2.

(D) PCE of control and SFA-PSCs fabricated under different RH.

(E) Long-term stability of unencapsulated device. The sample was stored in NIM's PV metrology lab with no inert-gas protection, no temperature control, no shading, and no deliberate light aging. The sample has been measured four times at different storage times, and the I-V characteristic curves and parameters are shown in the inset.

(F and G) Accelerated lifetime test of thermal stability (continuous heating at 85°C in N_2 atmosphere) (F) and continuous MPPT operational stability (1-sun equivalent white LED illumination) (G) of the control and SFA-devices.

and S43, further confirming the reproducibility and performance uniformity of the SFA-enabled large-area fabrication. To further evaluate the lateral uniformity of the large-area films, we performed spatially distributed PL measurements at nine uniformly sampled positions across the control and SFA-treated films (Figure S44). The SFA-film shows both a higher overall PL intensity and a markedly narrower position-to-position variation, together with lower and more concentrated $q\Delta V_3$ values, indicating improved active-area optoelectronic uniformity and more spatially homogeneous suppression of non-radiative recombination. However, during the area expansion process, the SFA device still experiences certain efficiency losses. These losses can be reasonably attributed to the increase in the series resistance, as well as the inevitable geometric dead zone losses introduced by the module lines (Table S7; Figure S45).

Reproducible PSCs under varying ambient conditions with different humidity is necessary for their industrialization. The SFA with hydrophobic stability finely regulates the perovskite crystallization through promoting the reaction formation, accelerating nucleation and crystallization with suppressed phase impurities, and hindering the perovskite decomposition in secondary crystallization, which effectively inhibits interference from moisture and is expected to improve the adaptability of corresponding PSCs to varying high-humidity ambient conditions. We compared the efficiency of PSCs prepared under RH of 25%, 50%, and 80%, respectively. The efficiency of control PSCs is sensitive to various levels of humidity: the average PCE decreased from 24.64% to

Please cite this article in press as: Yang et al., Thermally activated proton transfer enables air-processed perovskite solar cells approaching 27%, Joule (2026), https://doi.org/10.1016/j.joule.2026.102579

23.87%, then to 22.28%, as the RH increased from 25% to 50% and then to 80%, accompanied by the deteriorating reproducibility (Figure 4D). In comparison, the SFA-PSCs show an average PCE of 26.10% when the RH is 25%, and this average PCE shows a slight decrease to 25.99% when the RH increases to 50%. Even at the RH of 80%, the SFA-PSCs can obtain an average PCE of more than 25%, showing robust performance within the tested RH range together with improved reproducibility across independent fabrication batches (Figure S46).

We also evaluated the long-term stability of unencapsulated devices under different conditions. First, the unencapsulated PSCs were stored in ambient air with approximately 25% RH. After 4,000 h of aging, the PCE of control PSC decays to 58% of the initial value, while the PCE of SFA-PSC remains 99% of the initial PCE (Figure S47). Meanwhile, the unencapsulated SFA-PSCs were sent to an independent certified laboratory (National Institute of Metrology, China) for long-term stability monitoring and certificating. After 2,148 h of storage in laboratory air, the SFA-PSCs still maintain approximately 95% of their initial efficiency (Figures 4E and S48). A harsher condition of high temperature (85°C) was further applied to PSCs to monitor their heat stability. As shown in Figure 4F, the SFA-PSC can retain approximately 87% of its initial PCE after 750 h aging, while the control PSC only retains approximately 70%. Additional humidity-aging tests under sustained exposure at ~80% RH further confirm that SFA improves device tolerance to humid-air stress (Figure S49). The long-term operational stability of unencapsulated PSCs was tracked under continuous AM 1.5 G (100 mW cm^{-2}) illumination in a N_2 atmosphere at 50°C ± 5°C (Figure 4G). After 1,100 h, the SFA-PSCs can remain 91% of the initial PCE, whereas the control PSCs decay to 69% of the initial PCE after approximately 500 h. The optimized perovskite crystallization, immobilized FA^+, and the reduced defects should account for the remarkable photovoltaic performance and enhanced stability.

DISCUSSION

In summary, we develop a thermally activated proton-transfer strategy to address the performance limitations of air-processed α-$FAPbI_3$ PSCs under the coupled effects of moisture and thermal annealing. By introducing SFA as a stage-specific dynamic modulator, which can undergo proton transfer with thermally activated FA^+, we achieve precise regulation of perovskite crystallization across the process involving formation reaction, nucleation, primary crystallization, and secondary crystallization. This strategy delivers perovskite films with suppressed defects and improved optoelectronic properties, contributing to a champion PCE of 26.90% (certified 26.74%) of air-processed PSCs. The strategy is scalable, delivering 25.35% for 1 cm^2 devices and 21.03% for 8.2 cm^2 mini modules. Importantly, both the efficiency and durability are stringently validated by National Institute of Metrology, with unencapsulated devices maintaining >95% after 2,000 h ambient storage (ISOS-D-1). They also retained >91% after 1,100 h of operation under illumination (ISOS-L-1). This work provides a mechanistically grounded route toward scalable and climate-resilient perovskite photovoltaics.

METHODS

Materials

FTO glass (7 Ω sq^{-1}) was purchased from Shangyang Solar Energy Technology. (Suzhou, China). Thioglycolic acid (TGA, 98%), urea (>99.5%), and tin (II) chloride dihydrate ($SnCl_2{\cdot}2H_2O$, >99.995%) were purchased from Sigma-Aldrich. PbI_2 (purity: 99.999%) was purchased from Tokyo Chemical Industry (TCI). SFA was purchased from Aladdin. FAI, methylammonium chloride (MACl), and o-F-PEAI were purchased from Xi'an Yuri Solar. N, N-Dimethylformamide (DMF), dimethyl sulfoxide (DMSO), acetonitrile (ACN), chlorobenzene (CB), and isopropanol (IPA) were purchased from Sigma-Aldrich. Materials required for fabricating 2,2′,7,7′-tetrakis (N, N-di-p-methoxyphenylamine)-9,9′-spirobifluorene (spiro-OMeTAD) hole transport layer: tert-butylpyridine (tBP), li-bis(trifluoromethanesulfonyl)imid (Li-TFSI), and spiro-OMeTAD were purchased from Xi'an Yuri Solar. All the above materials are used directly after purchase and have not been further synthesized.

Device fabrication in ambient air

Solution preparation

Preparation of the SnO_2 chemical bath deposition (CBD) solution: 1.1 g $SnCl_2{\cdot}2H_2O$ (~12 mM) and 5 g urea were dissolved in 400 mL deionized water, and then 5 mL HCl (37 wt %) and 100 μL TGA were added into the solution. Preparation of the PbI_2 solution: 691.5 mg PbI_2 dissolved in 1 mL DMF:DMSO (14:1). For PbI_2 with SFA, the optimal addition amount is 1.0 mg/mL, the preparation method is consistent. Preparation of the ammonium salt solution: 90 mg FAI and 11 mg MACl dissolved in 1 mL IPA. Preparation of the o-F PEAI solution: 10 mM o-F PEAI dissolved in IPA. Preparation of the spiro solution: 72.3 mg spiro-OMeTAD in 1 mL CB mixed with 26.6 μL 4-tBP and 18 μL Li-TFSI (520 mg/mL in ACN).

Film deposition

Before use, the FTO was ultrasonically cleaned with deionized water, ethanol, and deionized water successively for 15 min. After the FTO is blown dry by a high-speed N_2 gun, a high-temperature-resistant adhesive is affixed to its necessary location. Before preparing tin oxide by chemical water bath, FTO was treated with ozone for 30 min to enhance its surface wettability. Then, the SnO_2 electron transport layers are prepared on FTO glass substrates by chemical bath deposition at 90°C for 4 h. Then, the FTO/SnO_2 substrates were removed from the solution, cleaned with deionized water and IPA ultrasonically, respectively, for 5 min, and annealed at 150°C for 1 h. After cooling to RT, PbI_2 solution was spin-coated on substrates at 1,500 rpm for 30 s and annealed at 70°C for 60 s. The ammonium salt solution was spin-coated on PbI_2 film at 2,000 rpm for 30 s and annealed at 150°C for 15 min. Then, o-F PEAI solution was spin-coated on the perovskite film at 4,000 rpm for 30 s without further annealing. For the charge transport layer, the spiro solution was also spin-coated at 4,000 rpm for 30 s. All of the above steps were performed in ambient air. The Au conductive layer (60 nm) was prepared by vacuum evaporation.

Characterization

The interaction of FAI and SFA is proved by 1H NMR (Ascend 600). XPS was measured by ESCALAB 250Xi system equipped

(Thermo Fisher Scientific). The SEM morphologies were examined using HITACHI SU8010. Fourier transform infrared (FTIR) spectra were characterized with Bruker INVENIO using attenuated total reflection (ATR) mode. The AFM results were obtained using an atomic force microscope (FMNanoview 1000). The XRD patterns were obtained on an X-ray diffractometer (D8 Advance, Bruker). Steady-state PL and TRPL were performed by an FLS980 spectrometer (Edinburgh Instrument). The *J-V* characteristics of PSCs were measured using a Keithley 2400 Source Meter with a power density of 100 mW/cm^2. The EQE spectra of PSCs were achieved using a EQE system (Enli Tech.).

DFT simulations

The density functional theory (DFT) calculations of clusters were performed using the Gaussian 16 program suite, including adsorption between FA^+ and SFA and the thermodynamic process of proton transfer. The different isomers were optimized with the B3LYP (Becke, 3-parameter, Lee-Yang-Parr) hybrid density functional[42–44] and the def2-TZVP basis set, a valence triple-zeta basis set with polarization functions developed by the Karlsruhe group.[45] Dispersion correction[46] and diffuse functions[47] were involved in all calculations, which may be necessary for the reliable description of the weak interaction. All energies reported in this work are total electronic energy with zero-point vibrational energy (ZPE) correction, except for the Gibbs free energy.

AIMD simulations

The AIMD simulations are conducted with the Vienna Ab initio Simulation Package (VASP).[48,49] The calculated model is set as a $25 \times 25 \times 25$ Å^3 box with FA^+ and SFA inside. The cutoff energy is 500 eV, and the k-point sampling was restricted to the Γ point only. The time step is set to 1 fs, and the total time is 9 ps. AIMD simulations are carried out at 100°C with the NVT (constant number of particles, volume, and temperature) ensemble.

RESOURCE AVAILABILITY

Lead contact

Further information and requests for resources and materials should be directed to and will be fulfilled by the lead contact, Meicheng Li (mcli@ncepu.edu.cn).

Materials availability

This study did not generate any new, unique materials.

Data and code availability

This study did not generate any datasets. All data needed to evaluate the conclusions in the paper are present in the paper or the supplemental information. All data are available from the corresponding authors upon reasonable request.

ACKNOWLEDGMENTS

This work is partially supported by the Beijing Natural Science Foundation (Z240024), the National Natural Science Foundation of China (grant nos. 52232008, 52402254, 52102245, and 22409061), the Beijing Natural Science Foundation (26JL001), the Key Research and Development Program sponsored by the Ministry of Science and Technology (MOST) (grant no. 2022YFB4200301), the project of China Three Gorges Corporation named key technologies of intelligent joint regulation and operation with grid connected friendly in power station group of wind, solar photovoltaic, and energy storage (WWKY-2021-0173), the Huaneng Group Headquarters Science and Technology Project (HNKJ20-H88), the Fundamental Research Funds for the Central Universities (2023MS042, 2023MS047, 2024MS036, and 2024MS039), and the NCEPU "Double First-Class" Program. The authors thank beamline BL14B1 and BL03HB at the Shanghai Synchrotron Radiation Facility (SSRF) for providing the beam time.

AUTHOR CONTRIBUTIONS

M.L., Y.Y., and H.H. conceived the idea. M.L., H.H., and Z.S. guided the work as supervisors. Y.Y., Z.L., and H.H. performed experimental designs, device fabrication, and data analysis. Y.C. participated in the DFT calculations. C.Y. and L.Y. participated in the device fabrication and some material and device characterizations. M.W., C.S., W.X., Q.Z., P.Z., S.D., S.Q., P.C., and Y.L. supported the measurement system construction, device fabrication, characterization, and discussions. Y.Y., H.H., and M.L. participated in manuscript writing and revising. All authors were involved in the discussions and approved the manuscript.

DECLARATION OF INTERESTS

The authors declare no competing interests.

SUPPLEMENTAL INFORMATION

Supplemental information can be found online at https://doi.org/10.1016/j.joule.2026.102579.

Received: January 26, 2026
Revised: April 8, 2026
Accepted: June 16, 2026

REFERENCES

1. Kojima, A., Teshima, K., Shirai, Y., and Miyasaka, T. (2009). Organometal halide perovskites as visible-Light sensitizers for photovoltaic cells. J. Am. Chem. Soc. *131*, 6050–6051. https://doi.org/10.1021/ja809598r.
2. Stranks, S.D., Eperon, G.E., Grancini, G., Menelaou, C., Alcocer, M.J.P., Leijtens, T., Herz, L.M., Petrozza, A., and Snaith, H.J. (2013). Electron-hole diffusion lengths exceeding 1 micrometer in an organometal trihalide perovskite absorber. Science *342*, 341–344. https://doi.org/10.1126/science.1243982.
3. Xiong, Z., Zhang, Q., Cai, K., Zhou, H., Song, Q., Han, Z., Kang, S., Li, Y., Jiang, Q., Zhang, X., et al. (2025). Homogenized chlorine distribution for >27% power conversion efficiency in perovskite solar cells. Science *390*, 638–642. https://doi.org/10.1126/science.adw8780.
4. Jeon, N.J., Noh, J.H., Yang, W.S., Kim, Y.C., Ryu, S., Seo, J., and Seok, S.I. (2015). Compositional engineering of perovskite materials for high-performance solar cells. Nature *517*, 476–480. https://doi.org/10.1038/nature14133.
5. Green, M.A., Ho-Baillie, A., and Snaith, H.J. (2014). The emergence of perovskite solar cells. Nat. Photon. *8*, 506–514. https://doi.org/10.1038/nphoton.2014.134.
6. Li, M., Jiao, B., Peng, Y., Zhou, J., Tan, L., Ren, N., Ye, Y., Liu, Y., Yang, Y., Chen, Y., et al. (2024). High-efficiency perovskite solar cells with improved interfacial charge extraction by bridging molecules. Adv. Mater. *36*, e2406532. https://doi.org/10.1002/adma.202406532.
7. Sidhik, S., Metcalf, I., Li, W.B., Kodalle, T., Dolan, C.J., Khalili, M., Hou, J., Mandani, F., Torma, A., Zhang, H., et al. (2024). Two-dimensional perovskite templates for durable, efficient formamidinium perovskite solar cells. Science *384*, 1227–1235. https://doi.org/10.1126/science.abq6993.
8. Yan, L., Huang, H., Cui, P., Du, S., Lan, Z., Yang, Y., Qu, S., Wang, X., Zhang, Q., Liu, B., et al. (2023). Fabrication of perovskite solar cells in

Please cite this article in press as: Yang et al., Thermally activated proton transfer enables air-processed perovskite solar cells approaching 27%, Joule (2026), https://doi.org/10.1016/j.joule.2026.102579

ambient air by blocking perovskite hydration with guanabenz acetate salt. Nat. Energy *8*, 1158–1167. https://doi.org/10.1038/s41560-023-01358-w.

9. Fu, S., Sun, N.N., Chen, H., Liu, C., Wang, X.M., Li, Y., Abudulimu, A., Xu, Y.Z., Ramakrishnan, S., Li, C.W., et al. (2025). On-demand formation of Lewis bases for efficient and stable perovskite solar cells. Nat. Nanotechnol. *20*, 772–778. https://doi.org/10.1038/s41565-025-01900-9.
10. Il Jake Choi, J.I.J., Ono, L.K., Cho, H., Kim, K.J., Kang, H.B., Qi, Y.B., and Park, J.Y. (2023). Pathways of water-induced lead-halide perovskite surface degradation: insights from in situ atomic-scale analysis. ACS Nano *17*, 25679–25688. https://doi.org/10.1021/acsnano.3c10611.
11. Meng, H.G., Mao, K.T., Cai, F.C., Zhang, K., Yuan, S.J., Li, T.Q., Cao, F.F., Su, Z.H., Zhu, Z.J., Feng, X.Y., et al. (2024). Inhibition of halide oxidation and deprotonation of organic cations with dimethylammonium formate for air-processed p-i-n perovskite solar cells. Nat. Energy *9*, 536–547. https://doi.org/10.1038/s41560-024-01471-4.
12. Wang, S.H., Miao, Z.P., Yang, J., Gu, Z.K., Li, P.W., Zhang, Y.Q., and Song, Y.L. (2024). Lead-chelating intermediate for air-processed phase-pure $FAPbI_3$ perovskite solar cells. Angew. Chem. Int. Ed. *63*, e202407192. https://doi.org/10.1002/anie.202407192.
13. Zou, Y., Yu, W.J., Guo, H.Q., Li, Q.Z., Li, X.D., Li, L., Liu, Y.L., Wang, H.T., Tang, Z.Y., Yang, S., et al. (2024). A crystal capping layer for formation of black-phase $FAPbI_3$ perovskite in humid air. Science *385*, 161–167. https://doi.org/10.1126/science.adn9646.
14. Kim, S.W., Moon, S.J., Kim, S.H., Yoo, J.J., Kim, D., Kim, B.S., and Jeon, N.J. (2023). Reducing humidity dependency of ambient-air-processed wide-bandgap inverted perovskite solar cells. ACS Energy Lett. *8*, 4777–4781. https://doi.org/10.1021/acsenergylett.3c01952.
15. Yang, G., Gu, H.Y., Yin, J., Fei, C.B., Shi, Z.F., Shi, X.Q., Ying, X.J., and Huang, J.S. (2025). Reductive cation for scalable wide-bandgap perovskite solar cells in ambient air. Nat. Sustain. *8*, 456–463. https://doi.org/10.1038/s41893-025-01529-5.
16. Cordero, F., Craciun, F., Trequattrini, F., Generosi, A., Paci, B., Paoletti, A.M., and Pennesi, G. (2019). Stability of cubic $FAPbI_3$ from X-ray diffraction, anelastic, and dielectric measurements. J. Phys. Chem. Lett. *10*, 2463–2469. https://doi.org/10.1021/acs.jpclett.9b00896.
17. Xing, Z., Fan, B.J., Meng, X.C., Li, D.X., Huang, Z.Q., Li, L.F., Zhang, Y.Y., Wang, F.Y., Hu, X.T., Hu, T., et al. (2024). Repairing humidity-induced interfacial degradation in quasi-2D perovskite solar cells printed in ambient air. Energy Environ. Sci. *17*, 3660–3669. https://doi.org/10.1039/D4EE00912F.
18. Yan, L.Y., Huang, H., Cui, P., Yang, Y.Y., Su, Z.H., Lu, Y., Wang, M., Lan, Z., Qu, S.J., Liu, B.Y., et al. (2025). Moisture-stable intermediate phase manipulation for efficient perovskite solar cells fabricated in ambient air. ACS Energy Lett. *10*, 5156–5164. https://doi.org/10.1021/acsenergylett.5c02481.
19. Ma, Y., Cai, H.Y., Liu, Y.J., He, B.Q., Zhang, H.F., Cheng, Y.Q., Liu, G.D., Zhao, J., Cheng, Y.B., and Zhong, J. (2025). Alleviation of precursor degradation induced by DMF/DMSO mixture for enhanced performance of perovskite solar cells. Angew. Chem. Int. Ed. *64*, e202504253. https://doi.org/10.1002/anie.202504253.
20. Hui, W., Chao, L.F., Lu, H., Xia, F., Wei, Q., Su, Z.H., Niu, T.T., Tao, L., Du, B., Li, D.L., et al. (2021). Stabilizing black-phase formamidinium perovskite formation at room temperature and high humidity. Science *371*, 1359–1364. https://doi.org/10.1126/science.abf7652.
21. Raval, P., Kennard, R.M., Vasileiadou, E.S., Dahlman, C.J., Spanopoulos, I., Chabinyc, M.L., Kanatzidis, M., and Manjunatha Reddy, G.N.M. (2022). Understanding instability in formamidinium lead halide perovskites: kinetics of transformative reactions at grain and subgrain boundaries. ACS Energy Lett. *7*, 1534–1543. https://doi.org/10.1021/acsenergylett.2c00140.
22. Ho, K., Wei, M.Y., Sargent, E.H., and Walker, G.C. (2021). Grain transformation and degradation mechanism of formamidinium and cesium lead iodide perovskite under humidity and light. ACS Energy Lett. *6*, 934–940. https://doi.org/10.1021/acsenergylett.0c02247.
23. Salim, K.M.M., Masi, S., Gualdrón-Reyes, A.F., Sánchez, R.S., Barea, E.M., Krecmarová, M., Sánchez-Royo, J.F., and Mora-Seró, I. (2021). Boosting long-term stability of pure formamidinium perovskite solar cells by ambient air additive assisted fabrication. ACS Energy Lett. *6*, 3511–3521. https://doi.org/10.1021/acsenergylett.1c01311.
24. Liu, Y.Q., Bu, T.L., Ono, L.K., Tong, G.Q., Zhang, H., and Qi, Y.B. (2021). Phase aggregation suppression of homogeneous perovskites processed in ambient condition toward efficient light-emitting diodes. Adv. Funct. Mater. *31*, 2103399. https://doi.org/10.1002/adfm.202103399.
25. Zhu, H.W., Teale, S., Lintangpradipto, M.N., Mahesh, S., Chen, B., McGehee, M.D., Sargent, E.H., and Bakr, O.M. (2023). Long-term operating stability in perovskite photovoltaics. Nat. Rev. Mater. *8*, 569–586. https://doi.org/10.1038/s41578-023-00582-w.
26. Chu, Z., Fan, B., Zhao, Y., Xie, Y., Luo, Y., Li, J., Gong, C., Zhang, Y., Meng, X., Chen, Y., et al. (2025). Laser annealing enables rapid, degradation-free ambient processing of perovskite solar modules. Science *390*, 905–910. https://doi.org/10.1126/science.adx9650.
27. Yang, Y., Huang, H., Yan, L., Cui, P., Lan, Z., Sun, C., Du, S., Wang, X., Yao, C., Qu, S., et al. (2024). Compatible soft-templated deposition and surface molecular bridge construction of SnO_2 enable air-fabricated perovskite solar cells with efficiency exceeding 25.7%. Adv. Energy Mater. *14*, 2400416. https://doi.org/10.1002/aenm.202400416.
28. Chen, R., Wang, J.A., Liu, Z.H., Ren, F.M., Liu, S.W., Zhou, J., Wang, H.X., Meng, X., Zhang, Z., Guan, X.Y., et al. (2023). Reduction of bulk and surface defects in inverted methylammonium- and bromide-free formamidinium perovskite solar cells. Nat. Energy *8*, 839–849. https://doi.org/10.1038/s41560-023-01288-7.
29. Du, S., Huang, H., Lan, Z., Cui, P., Li, L., Wang, M., Qu, S., Yan, L., Sun, C., Yang, Y., et al. (2024). Inhibiting perovskite decomposition by a creeper-inspired strategy enables efficient and stable perovskite solar cells. Nat. Commun. *15*, 5223. https://doi.org/10.1038/s41467-024-49617-y.
30. Zhang, H., Xiang, W., Zuo, X., Gu, X., Zhang, S., Du, Y., Wang, Z., Liu, Y., Wu, H., Wang, P., et al. (2022). Fluorine-containing passivation layer via surface chelation for inorganic perovskite solar cells. Angew. Chem. Int. Ed. *62*, e202216634. https://doi.org/10.1002/anie.202216634.
31. Shi, P.J., Ding, Y., Ding, B., Xing, Q.Y., Kodalle, T., Sutter-Fella, C.M., Yavuz, I., Yao, C.L., Fan, W., Xu, J.Z., et al. (2023). Oriented nucleation in formamidinium perovskite for photovoltaics. Nature *620*, 323–327. https://doi.org/10.1038/s41586-023-06208-z.
32. Li, F.Z., Deng, X., Shi, Z.S., Wu, S.F., Zeng, Z.X., Wang, D., Li, Y., Qi, F., Zhang, Z.M., Yang, Z.B., et al. (2023). Hydrogen-bond-bridged intermediate for perovskite solar cells with enhanced efficiency and stability. Nat. Photon. *17*, 478–484. https://doi.org/10.1038/s41566-023-01180-6.
33. Ruan, S., McMeekin, D.P., Fan, R., Webster, N.A.S., Ebendorff-Heidepriem, H., Cheng, Y.B., Lu, J.F., Ruan, Y.L., and McNeill, C.R. (2020). Raman spectroscopy of formamidinium-based lead halide perovskite single crystals. J. Phys. Chem. C *124*, 2265–2272. https://doi.org/10.1021/acs.jpcc.9b08917.
34. Lin, L.Y., Jones, T.W., Yang, T.C.J., Li, X.Y., Wu, C.C., Xiao, Z.C., Li, H.J., Li, J.H., Qian, J.W., Lin, L., et al. (2024). Hydrogen bonding in perovskite solar cells. Matter *7*, 38–58. https://doi.org/10.1016/j.matt.2023.10.013.
35. Kubicki, D.J., Stranks, S.D., Grey, C.P., and Emsley, L. (2021). NMR spectroscopy probes microstructure, dynamics and doping of metal halide perovskites. Nat. Rev. Chem. *5*, 624–645. https://doi.org/10.1038/s41570-021-00309-x.
36. He, J.C., Sheng, W.P., Liu, K.K., Cai, Q.Q., Zhong, Y., Tan, L.C., and Chen, Y.W. (2025). Unraveling the reaction dynamics mechanism and thermodynamic pathway of lead iodide and organic cations in the two-step sequential deposition process. Energy Environ. Sci. *18*, 6983–7004. https://doi.org/10.1039/D5EE01294E.
37. Wang, Z.P., Lin, Q.Q., Chmiel, F.P., Sakai, N., Herz, L.M., and Snaith, H.J. (2017). Efficient ambient-air-stable solar cells with 2D-3D heterostructured butylammonium-caesium-formamidinium lead halide perovskites. Nat. Energy *2*, 17135. https://doi.org/10.1038/nenergy.2017.135.

38. Liu, S.W., Miao, T.Y., Wang, J.N., Zhang, Y., Chen, R., Lei, X., Qin, W.M., Zhu, Z.J., Lu, L.L., Chen, Z.H., et al. (2026). Solvated-intermediate-driven surface transformation of lead halide perovskites. Nat. Energy *11*, 109–120. https://doi.org/10.1038/s41560-025-01912-8.

39. Sun, Q., Duan, S.C., Liu, G., Meng, X.X., Hu, D., Deng, J.G., Shen, B., Kang, B.A., and Silva, S.R.P. (2023). Porous lead iodide layer promotes organic amine salt diffusion to achieve high performance p-i-n flexible perovskite solar cells. Adv. Energy Mater. *13*, 2301259. https://doi.org/10.1002/aenm.202301259.

40. Liu, M.C., Zhang, J.Y., Qin, S.C., Miao, X.D., Yuan, M., Liu, Z., Wang, Y.Y., Feng, Y.S., Jiang, X., Wu, R.H., et al. (2024). Efficient and stable p-i-n perovskite solar cells enabled by in situ functional group conversion. J. Am. Chem. Soc. *146*, 32105–32116. https://doi.org/10.1021/jacs.4c13248.

41. Huang, H., Cui, P., Chen, Y., Yan, L., Yue, X., Qu, S., Wang, X., Du, S., Liu, B., Zhang, Q., et al. (2022). 24.8%-efficient planar perovskite solar cells via ligand-engineered TiO_2 deposition. Joule *6*, 2186–2202. https://doi.org/10.1016/j.joule.2022.07.004.

42. Becke, A.D. (1988). Density-functional exchange-energy approximation with correct asymptotic behavior. Phys. Rev. A Gen. Phys. *38*, 3098–3100. https://doi.org/10.1103/PhysRevA.38.3098.

43. Becke, A.D. (1993). Density-functional thermochemistry. III. The role of exact exchange. J. Chem. Phys. *98*, 5648–5652. https://doi.org/10.1063/1.464913.

44. Lee, C., Yang, W., and Parr, R.G. (1988). Development of the colle-salvetti correlation-energy formula into a functional of the electron density. Phys. Rev. B Condens. Matter *37*, 785–789. https://doi.org/10.1103/PhysRevB.37.785.

45. Weigend, F., and Ahlrichs, R. (2005). Balanced basis sets of split valence, triple zeta valence and quadruple zeta valence quality for H to Rn: Design and assessment of accuracy. Phys. Chem. Chem. Phys. *7*, 3297–3305. https://doi.org/10.1039/B508541A.

46. Grimme, S., Antony, J., Ehrlich, S., and Krieg, H. (2010). A consistent and accurate ab initio parametrization of density functional dispersion correction (DFT-D) for the 94 elements H-Pu. J. Chem. Phys. *132*, 154104. https://doi.org/10.1063/1.3382344.

47. Zheng, J.J., Xu, X.F., and Truhlar, D.G. (2011). Minimally augmented Karlsruhe basis sets. Theor. Chem. Acc. *128*, 295–305. https://doi.org/10.1007/s00214-010-0846-z.

48. Kresse, G., and Furthmüller, J. (1996). Efficiency of ab-initio total energy calculations for metals and semiconductors using a plane-wave basis set. Comput. Mater. Sci. *6*, 15–50. https://doi.org/10.1016/0927-0256(96)00008-0.

49. Kresse, G., and Joubert, D. (1999). From ultrasoft pseudopotentials to the projector augmented-wave method. Phys. Rev. B *59*, 1758–1775. https://doi.org/10.1103/PhysRevB.59.1758.